Sensitivity analysis of initial conditions for contrail formation with ground-based camera imagery

By T. Ferreira, R. Quibén Figueroa†, M. Soler Arnedo† AND C. Gorlé

This study combines all-sky ground-based camera imagery of contrails with the Schmidt –Appleman criterion (SAC) approach and large-eddy simulations (LES) based on a contrail-adapted solver to assess the predictability of early-stage contrail formation. A variance-based Sobol sensitivity analysis across 764 flights identifies atmospheric temperature as the dominant first-order contributor to prediction variability based on the SAC and initial conditions for LES (LES-IC) approaches. A contrail probability analysis of 248 visually verified flights shows consistent results between the two approches, but a tendency to overpredict contrail formation, likely due to simplified plume-mixing assumptions and temperature biases in weather reanalysis data. A false-negative case study, in which all-sky imagery revealed a visible contrail that both models failed to predict, futher illustrates the impact of flight altitude and thermodynamic inaccuracies. These results highlight the need for improved meteorological and altitude data fidelity and more realistic bypass-flow representations in contrail models.

1. Introduction

Aircraft condensation trails (contrails) are among the most uncertain non-CO_2 effects of aviation on climate (Lee *et al.* 2021). When atmospheric conditions favor ice supersaturation, contrails may persist and spread into cirrus-like layers that modify the Earth's radiative balance (Kärcher 2018).

Predicting their formation remains challenging as it depends on accurate and timely meteorological data. Whereas contrail persistence can be assessed through satellite observations (Gierens *et al.* 2020), the early formation stage typically exhibits optical depths too small for reliable detection. All-sky ground-based camera imagery on the other hand offers a higher temporal and spatial resolution in the visible range necessary to capture these initial stages of contrail formation. Previous studies have had different degrees of success with this approach, using sky-imaging networks to identify and classify contrail occurrences under diverse meteorological conditions (Mannstein *et al.* 2010; Schumann *et al.* 2013; Low *et al.* 2025).

The prediction of contrail formation is typically based on the Schmidt–Appleman criterion (SAC) (Schumann 1996), which determines whether the exhaust–atmosphere mixing line intersects the water vapor saturation curve with respect to water, neglecting the role of bypass flow interaction, plume dilution, and small-scale turbulent mixing.

To capture some of these processes explicitly, large-eddy simulations (LES) can be employed to resolve the jet–vortex dynamics and the formation of the early contrail ice crystals (e.g., Paoli *et al.* 2004; Naiman *et al.* 2011; Paoli *et al.* 2013; Lewellen 2020). However, such high-fidelity simulations are sensitive to system uncertainties in initial conditions and atmospheric properties.

† Aerospace Engineering Department, Universidad Carlos III de Madrid, Spain

In this study, first presented at EGU General Assembly 2025 (Quibén Figueroa *et al.* 2025), we combine the strengths of both modeling approaches to assess the predictability of the early stages of contrail formation. We apply a variance-based Sobol sensitivity analysis to quantify how uncertainties in atmospheric and engine parameters propagate to the predicted thermodynamic state and contrail formation likelihood based on the SAC and LES initial conditions (LES-IC). We further perform a contrail probability evaluation by linking modeling results to visual observations from all-sky ground-based cameras of a set of flight segments.

The datasets and methods employed for contrail observation, flight tracking, meteorological characterization, and contrail formation modeling are described in Section 2. The results are presented in Section 3, including the detailed study of a single flight false-negative case (where all-sky images show a visible contrail but modeling approaches do not predict a contrail) a global sensitivity analysis, and a contrail probability evaluation over multiple flight segments observed over Paris and Toulouse. Finally, we summarize our conclusions and future work perspectives in Section 4.

2. Data and methods

We describe how we gather and interpolate aircraft and atmospheric data to characterize the flight trajectories within the sky area captured by ground-based cameras. We then visually inspect this sky imagery for contrails and compare our findings with contrail formation criteria, high-fidelity simulations, and a global sensitivity analysis.

2.1. *Contrail observation data: ground-based camera imagery*

Contrail observation imagery was either shared by EUROCONTROL from Reuniwatt's all-sky ground-based cameras or bought directly from Reuniwatt by Universidad Carlos III de Madrid for research purposes.

These ground-based cameras provide a coverage area of 72 km^2. They produce monochrome images with low noise, featuring a resolution of 4 megapixel, an effective size of 2064 x 2064 pixels, and a 8-bit monochrome dynamic range. For the purposes of contrail tracking, the camera images are calibrated based on the sun optical distortion and camera orientation, as illustrated in Figure 1.

The frequency between camera shots corresponds to $f_{\mathrm{cam}} = 30$ s. This temporal resolution is unable to resolve the jet phase i.e., the first stage of contrail formation in which the dominating fluid motion is the axial jet exhaust mixing with the atmosphere—whose time-scale is in the order of seconds, with $t_{\mathrm{jet}} < 10$ s. The subsequent vortex phase—where the aircraft wake vortices define the contrail plume dynamics—has a duration in the order of $t_{\mathrm{vortex}} = O(100)$ s.

In this way, although insufficient to resolve the jet and vortex phases of contrail formation, the camera frequency f_{cam} allows observation of the end of the vortex phase and the initial dissipation regime of contrails, which is in the order of $t_{\mathrm{dissip}} = O(1000)$ s.

However, the observation time window is limited by the period during which the contrail remains within the camera's field of view, which can vary widely due to wind advection. In most cases, contrails remain visible for approximately 15 min (≈1000 s), although some can be tracked for up to 60 min, depending on wind speed and direction.

The following section explains how aircraft trajectories from air traffic ADS-B data are superimposed onto the all-sky images to track contrail formation, as shown in Figure 1.

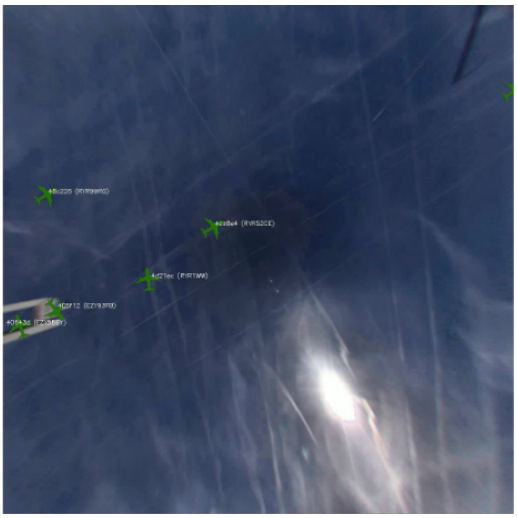

FIGURE 1. Ground-based camera image calibrated and overlapped with aircraft flight trajectories from ADS-B data.

Region	**Latitude**	**Longitude**	**Date**	**Start (UTC)**	**End (UTC)**
Toulouse	43.1–44.0°N	1.05–1.95°E	2024-01-29	08:00	18:30
			2024-01-30	08:00	18:30
Paris	48.2–49.0°N	1.9–2.8°E	2024-01-24	09:00	09:45
			2024-01-26	13:00	15:00
			2024-01-29	07:30	09:30
			2024-01-31	16:00	16:30

TABLE 1. Geographical bounds and time windows of contrail ground-based camera observations.

2.2. *Flight trajectory data*

Aircraft trajectory information were obtained from ADS-B flight-tracking data, which is made available by the OpenSky Network (Schäfer *et al.* 2014) through the Python library traffic (Olive 2019). Historical flight data were queried and constrained by spatial bounds (longitude–latitude) and time intervals—10 min windows buffered by 10 min, in Coordinated Universal Time (UTC)—corresponding to contrail observations described in Table 1. An example of a 10 min flight data extraction is displayed in Figure 2(a).

To focus on the cruise level, relevant for contrail formation, only airborne segments were selected (onground = false) and an additional filter excluded the low-altitude phases (below 8,000 m). We extract the following data for each flight: callsign (flight ID), timestamp, longitude, latitude, altitude, and GPS altitude. The reference altitude is given by the barometric altimeter and is generally considered more accurate for cruise levels than the GPS (global positioning system) altitude (also known as geometric altitude). We note that we use a median filter on the altitude profiles before interpolating with the atmospheric data to clean any remaining signal noise.

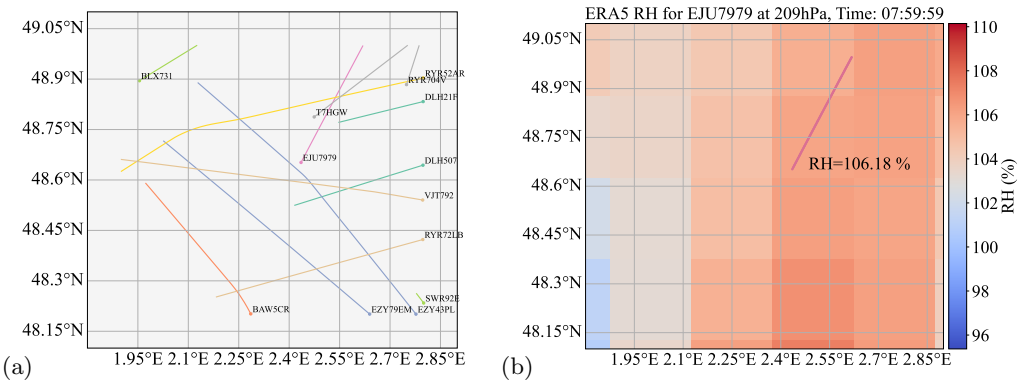

FIGURE 2. Example of (a) extracting flight trajectory data and (b) interpolating each flight trajectory onto weather data—in this case for the relative humidity with respect to ice RH_i.

2.3. *Atmospheric reanalysis data*

The atmospheric data are obtained from ERA5, the fifth-generation reanalysis of the European Centre for Medium-Range Weather Forecasts (ECMWF), which gives hourly, global estimates of the Earth's atmosphere thermodynamic variables on pressure levels. The spatial resolution corresponds to 0.25° longitude × 0.25° latitude over 37 pressure levels and at a 1 h temporal resolution. The dataset is available through the Copernicus Climate Data Store (CDS), which we access via the Python cdsapi library.

We extract the relevant atmospheric data for each day and region, as defined in Table 1, for pressure levels between 100 and 400 hPa. Among many available variables, we focus on the ones relevant to our criteria for contrail formation, which are temperature and relative humidity.

Since the ADS-B exchange data do not include pressure, we convert the (barometric) altitude to pressure using the International Standard Atmosphere (ISA) static atmosphere model. This pressure value is used to define the pressure level for which we interpolate the atmospheric data for each flight, in addition to the latitude and longitude of the trajectory and the time of day. The result for the relative humidity is shown in Figure 2(b). Following the interpolation, we use a correction for the relative humidity over ice based on in-situ measurements from the In-service Aircraft for a Global Observing System (IAGOS) dataset elaborated by Teoh *et al.* (2022).

2.4. *Contrail formation criterion: the SAC approach*

The SAC is frequently used to determine the thresholds for contrail formation by modeling the cooling of the hot vapor–laden plume in the atmosphere (Schumann 1996, 2012). The SAC approach computes the thermodynamic mixing line representing the cooling of the plume by assuming isobaric mixing and the same rate of heat and vapor diffusion. Contrail formation is bound to occur if this mixing line crosses at some point the curve defined by the water vapor saturation with respect to water, as described in Figure 5 in Section 3.1. This crossing implies that the vapor surrounding the particles within the jet plume is saturated over water, allowing it to condense onto the particles and freeze, as the temperature is usually below or close to the homogeneous freezing temperature. The slope of the jet–atmosphere thermodynamic mixing line is defined,

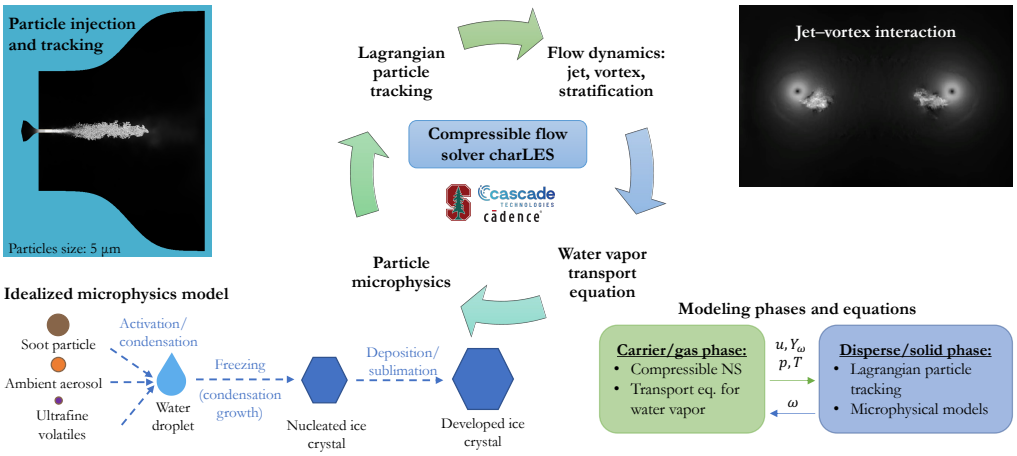

FIGURE 3. Sketch of charLES ideal gas solver adaptation for contrail simulations.

$$G_{\mathrm{SAC}} = \frac{c_p p_{\mathrm{atm}}}{\epsilon} \frac{\mathrm{EI}_{\mathrm{H_2O}}}{(1-\eta)Q}, \tag{2.1}$$

where $c_p = 1004\ \mathrm{J\,kg^{-1}\,K^{-1}}$ is the heat capacity of air at constant pressure, $\epsilon = M_{\mathrm{air}}/M_{\mathrm{H_2O}} - 1$ where $M_{\mathrm{air}} = 28.97\ \mathrm{g\,mol^{-1}}$ and $M_{\mathrm{H_2O}} = 18.02\ \mathrm{g\,mol^{-1}}$ are the molecular weights of dry air and water, respectively, $\mathrm{EI}_{\mathrm{H_2O}} = 1.30$ is water vapor emission index $\mathrm{kg\,kg^{-1}}$ fuel, $\eta = 35\%$ is the overall propulsive efficiency, and $Q = 43.1 \cdot 10^6\ \mathrm{MJ\,kg^{-1}}$ is the fuel heating value of kerosene.

2.5. *High-fidelity simulation of contrails: LES*

We also perform LES of contrail formation to gain further insight into the potential of validating contrail modeling approaches with ground-based camera imagery. Our LES tool is the nextgen CPU version of charLES from Cadence.

The charLES code is a 3D massively parallel, finite volume, compressible LES flow solver on Voronoi-like polyhedral mesh cells (e.g., Brès *et al.* 2018). This solver uses a second-order central scheme for the spatial discretization of the carrier phase and an explicit three-stage Runge–Kutta method for the temporal discretization of both the carrier and disperse phases.

We have adapted the charLES ideal gas solver to simulate contrails by adding a transport equation for water vapor and microphysical models to represent particle pathways into an ice crystal. The jet and vortex fields formed behind an aircraft are initialized based on hyperbolic tangent profiles of the core and bypass flow and Lamb–Oseen vortices, respectively. The resulting solver is illustrated in Figure 3. Making use of this solver's Eulerian–Lagrangian framework, the Eulerian grid solves the compressible Navier–Stokes equations of the gas phase (air and water vapor), and the Lagrangian particle tracking method handles the flow particles representing atmospheric aerosol, water droplets, and ice crystals. The particles are assumed to be passive tracers due to their low Stokes number during early contrail formation (10^{-9} to 10^{-5}), and a mass source term couples the water vapor transport equation (gas) with the microphysical models (particles).

This tool has been used for simulations of the jet and vortex phases of contrail formation in previous research on the effect of Crow instability and sensitivity analysis of

$\mathrm{RH_i}$	95.5	relative humidity with respect to ice (%)
T_{atm}	228.6	atmospheric temperature (K)
p_{atm}	314.8	atmospheric pressure (hPa)
M	0.70	Mach number
h_{baro}	8839.2	barometric altitude (m)
h_{geo}	9105.9	geometric (GPS-based) altitude (m)

TABLE 2. Atmospheric and trajectory data for Flight EJU978X (Paris, Jan 29, 2024).

conventional and hydrogen aircraft on the number of ice crystals (Ferreira *et al.* 2024*b*,*a*, 2025). The reader is directed to Ferreira *et al.* (2024*a*) for more details on the simulation framework for early contrail formation.

For the purposes of the present study, our focus is on contrail formation that is comparable with available ground-based camera imagery. As such, we use both known and assumed atmospheric and engine parameters for initialization of the temperature, pressure, and water vapor fields. Similarly to the SAC approach and previous LES of contrails, we use the same turbulent Prandtl and Schmidt number—the turbulent Lewis number is thus unity—and we obtain close to an equivalent rate of heat and water vapor diffusion (Paoli *et al.* 2013).

As such, tracking the particles inside the plume, we obtain a profile close to a mixing line that can be characterized by a slope G_{LES},

$$G_{\mathrm{LES}} = \frac{p_{v_{\mathrm{jet}}} - p_{v_{\mathrm{atm}}}}{T_{\mathrm{jet}} - T_{\mathrm{atm}}}, \tag{2.2}$$

defined by the atmospheric and jet values for the vapor pressure and temperature, $p_{v_{\mathrm{atm}}}$, T_{atm}, $p_{v_{\mathrm{jet}}}$, and T_{jet}, respectively. Although G_{LES} is simple to compute, there are a few terms involved in computing $p_{v_{\mathrm{jet}}}$, such as the radius of the engine core jet flow r_{core}, velocity $V_{\mathrm{xx,core}}$, fuel mass flow rate $\dot{m}_{\mathrm{fuel}}$, water vapor emission index $\mathrm{EI_{H_2O}}$, flight Mach number M, and temperature of the core flow T_{core}, which add to the uncertainty.

3. Results

We first analyze in detail a false-negative flight under both the LES modeling framework and the SAC approach for contrail formation. Building on this test case, we then perform a global sensitivity analysis and a contrail probability study over a larger set of flight segments observed over Paris and Toulouse.

3.1. *Large-eddy simulation: Flight EJU978X*

Our first step was to analyze a false-negative case, in which contrail formation is observable through ground-based camera imagery but the contrail formation criterion, the SAC, is not satisfied. We selected the Flight EJU978X, flown over Paris on January 29, 2024. Details on the averaged atmospheric flight conditions and aircraft parameters used to initialize the LES are presented in Tables 2 and 3, respectively.

Our first run did not produce any ice crystals—the mixing line does not cross the vapor saturation curve so it cannot trigger any formation of water droplets and ice crystals. As a next step, we modified the engine parameters, fuel mass flow and exit temperature, artificially imposing an equivalent higher overall propulsive efficiency. This

Aircraft parameters		
Model	Airbus A320-type	
Maximum takeoff weight	77 000	kg
Wingspan	35.8	m
Engine spacing	11.5	m

Engine parameters		
Model	CFM56-type	
Core radius	0.305	m
Total radius	0.755	m
Mass flow rate	0.32	kg s^{-1}

TABLE 3. Aircraft and engine parameters for Flight EJU978X.

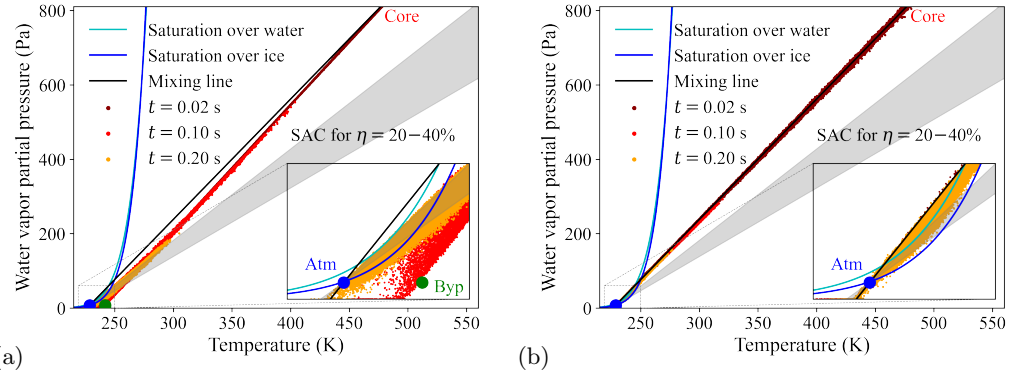

FIGURE 4. Particle mixing results for Flight EJU978X from LES (a) with and (b) without bypass flow, along with water vapor saturation curves and the jet–atmosphere mixing line for comparison.

greater efficiency, when compared to the SAC slopes, is higher than 40%. Even then, only a few ice crystals form, insufficient to represent a visible contrail. We can interpret these results in Figure 4(a)—although the theoretical mixing line does cross the vapor saturation over water, the presence of the colder, less humid bypass flow causes a deviation from this line. As a result, only a few particles are surrounded by saturated vapor with respect to water.

Following this, we reduced the bypass flow and increased the number of soot particles; still, there were too few ice crystals to form a contrail. Finally, in the last simulation we removed the bypass flow from the Figure 4(a) case to follow more exactly the mixing line. As a result, a visible contrail is formed (with an optical depth greater than 0.2) as a more significant number of ice crystals are nucleated. For comparison, this is shown in Figure 4(b), where a much larger number of particles are in the region of vapor saturation with respect to water, thus forming water droplets and ice crystals as the temperature decreases.

Since the SAC approach assumes the last stages of a mixing jet–atmosphere flow, it is not surprising that the particle mixing we see toward the low atmospheric temperatures in Figure 4(a) is closer to the mixing lines of a realistic propulsive efficiency. The point to highlight is that, with this understanding of how the bypass flow changes the mixing and the formation of ice crystals, we can proceed to a more comprehensive sensitivity analysis. We can perform this analysis by focusing on the initial conditions used to set-up the LES without the need to run hundreds of LES for each flight case.

The barometric and GPS altitudes differ by 3%, as shown in Table 2. In general,

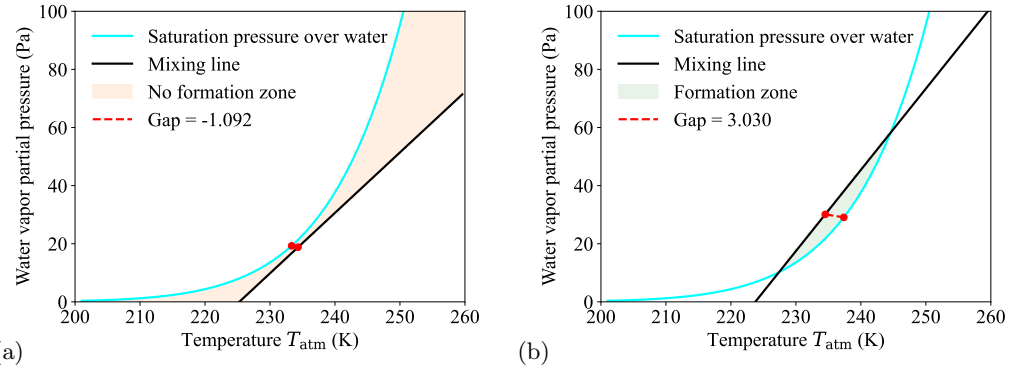

FIGURE 5. Two examples from the Saltelli sampling analysis for which the parameter combination leads to a mixing indicative of (a) contrail formation, and of (b) no contrail formation.

the barometric altitude is considered the most accurate for cruise level, which in this case, corresponds to a lower altitude, implying a smaller chance of contrail formation. Nevertheless, we analyzed the atmospheric data and compared pressure levels with a $\pm 5\%$ variation. The result of interpolating at these different pressures, and therefore altitudes, is a temperature variation of ± 2.8 K. For reference, a temperature lower by 2 K is sufficient to trigger contrail formation in the SAC approach. This variation in pressure/altitude would therefore be able to justify the formation of contrail. As such, the next step of this work is to explore the effect of a larger parameter space on contrail formation modeling approaches by means of a global sensitivity analysis.

3.2. *Global sensitivity analysis: Flight EJU978X*

We perform a variance-based global sensitivity analysis to infer qualitatively the influence of the initial conditions on contrail formation. We analyze contrail formation both based on the SAC through Eq. (2.1) and on the LES-IC through Eq. (2.2). As such, the input parameters differ between these analyses. The sensitivity analysis is conducted using the Sobol method (Sobol 2001; Lu *et al.* 2025) with Saltelli sampling, which decomposes the output variance into individual variable contributions and their interactions.

We selected as quantity of interest (QoI) the maximum distance (gap) perpendicular from the mixing line to the vapor saturation curve over water and use 2^{15} samples. A large positive gap indicates a higher potential for forming contrails, with the opposite being true, as illustrated in Figure 5. We choose this quantity based on the outcomes from the LES of contrails shown in Figure 4.

The input parameters for the SAC approach are atmospheric and other variables from Eq. (2.1), which yield

$$\theta_{\mathrm{SAC}} = \{T_{\mathrm{atm}}, \mathrm{RH_i}, p_{\mathrm{atm}}, \mathrm{EI_{H_2O}}, \eta, Q\}. \tag{3.1}$$

The input parameters for the LES-IC analysis are less direct since we have to consider the core flow to obtain the mixing line slope described in Eq. (2.2) for

$$\theta_{\mathrm{LES}} = \{T_{\mathrm{atm}}, \mathrm{RH_i}, p_{\mathrm{atm}}, \mathrm{EI_{H_2O}}, r_{\mathrm{core}}, \dot{m}_{\mathrm{fuel}}, T_{\mathrm{core}}, V_{\mathrm{xx,core}}, M\}. \tag{3.2}$$

The range of uncertainties is prescribed within $\pm 5\%$ of the nominal value for all the

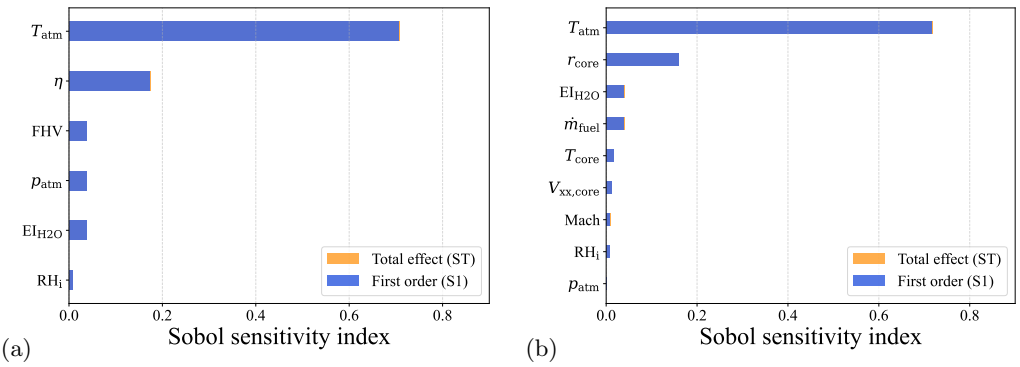

FIGURE 6. First-order and total effect indices for the input parameters of the Sobol sensitivity analysis for the (a) SAC and (b) LES-IC approaches.

parameters except for the atmospheric temperature T_{atm}. A smaller uncertainty of $\pm 1\%$ (approximately ± 2 K) is assigned to T_{atm}.

3.2.1. *Analysis of Sobol sensitivity indices*

The Sobol sensitivity analysis shows that the first-order (SI) indices dominate in Figure 6, with second- and higher-order interaction terms represented in the total effects (ST) indices, contributing negligibly to the total variance.

The atmospheric temperature emerges as the dominating contributor to the variance of the QoI for both approaches, the SAC and LES-IC. Even with a reduced input variation of $\pm 1\%$, this parameter strongly influences the likelihood of contrail formation in these modeling approaches. The importance of the atmospheric temperature is verified whether we use as QoI the distance to the saturation state or the area of the contrail formation zone. This strong sensitivity of contrail prediction approaches to atmospheric temperature underscores the importance of accurate aircraft pressure and altitude measurements, as well as the need to minimize systematic temperature biases in weather reanalysis databases.

For the SAC sensitivity analysis, the overall propulsive efficiency comes as the second largest first-order effect, as it has a large influence on the slope of the mixing, as evident in Figure 4. The initial conditions for LES, secondarily to the atmospheric temperature, show a high dependence on the engine parameters. The radius of the engine core influences the QoI as it changes the initial water vapor concentration in the core flow, where higher quantities lead to a steeper slope.

Although the present analysis is limited to a narrow range of aircraft and engine parameters, extending this parameter space is expected to lead to stronger sensitivities, but the atmospheric temperature is likely to remain a dominant first-order effect parameter.

3.2.2. *Probability of contrail formation*

The thermodynamic mixing lines obtained from the Saltelli sampled input space using the barometric altitude are shown in Figure 7. From these analyses, we estimate the probability of a contrail-forming event, $P_{contrail}$, which is defined as the occurrence of a crossing between the thermodynamic mixing line and the water vapor saturation curve, as exemplified in Figure 5. For the SAC approach, the probability of contrail formation is $P_{contrail} = 41\%$ when based on the barometric altitude and 78% when based on the GPS altitude. For LES-IC, the corresponding probabilities are 52% and 93%, respectively.

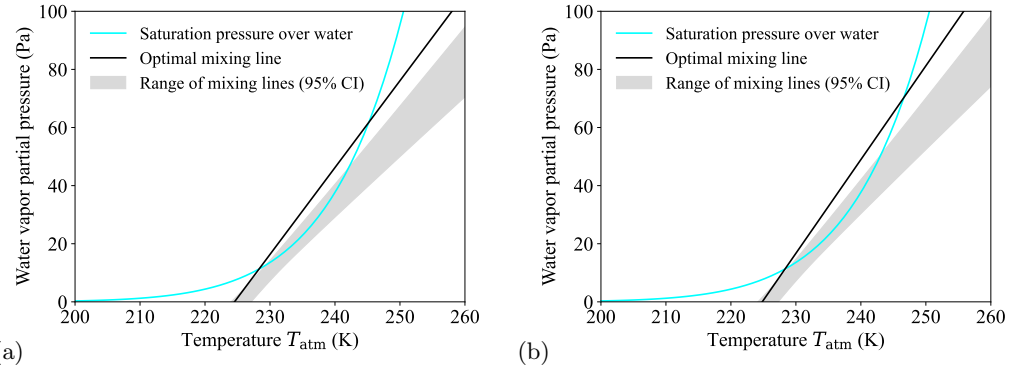

FIGURE 7. Optimal and 95% confidence interval (CI) range of mixing lines from Sobol sensitivity analysis for the (a) SAC and (b) LES-IC approaches.

Flight EJU978X	$P_{contrail}$ **based on**	
Modeling approach	*Barometric altitude*	*GPS altitude*
Schmidt–Appleman criterion (SAC)	41%	78%
Initial conditions for LES (LES-IC)	52%	93%

TABLE 4. Probability of contrail formation, $P_{contrail}$, based on altitude reference for the SAC and LES-IC approaches.

The outcomes are summarized in Table 4, highlighting the strong dependence of the predicted contrail likelihood on the altitude reference—consistent with the large sensitivity to small pressure and temperature variations—as seen in Section 3.1 and Figure 6.

3.3. *Contrail probability analysis: set of flights over Paris and Toulouse*

Finally, we apply our contrail probability framework to the remaining set of flights listed in Table 1. From these cases, we used the all-sky ground-based camera images described in Section 2.1 to associate observed contrail formation with corresponding flight trajectories. In total, 248 flights have been manually cataloged as either (i) forming a visible contrail along their tracked flight path (Contrail) or (ii) not exhibiting a visible contrail within the corresponding temporal and spatial observation window (No contrail).

The outcomes of this study are presented in Table 5, in which both the SAC and LES-IC approaches yield very similar results. This convergence can be attributed to the limited variability of engine parameters. While the initial conditions for the LES framework in principle allow for a broader parameter space, the SAC formulation accounts primarily for overall propulsive efficiency, which may lead to a narrower range of variability, independent of aircraft size. Therefore, the apparent similarity between both approaches may be a consequence of the constrained sampling of engine parameters.

The confusion matrix in Table 5 indicates a systematic overprediction of contrail formation, with most misclassified cases corresponding to false-positives, where no contrail

	SAC prediction		
Observed	Contrail	No contrail	Total
Contrail	92	2	94
No contrail	153	1	154
Total	245	3	248

	LES-IC prediction		
Observed	Contrail	No contrail	Total
Contrail	93	1	94
No contrail	153	1	154
Total	246	2	248

TABLE 5. Comparing predicted and observed contrail formation over 248 occurrences.

is observable on ground-based camera images but the modeling approaches predict the formation of one. Several factors may contribute to this behavior, such as

(*a*) the formation criterion is defined solely by the crossing of the water vapor saturation curve, neglecting the effect of bypass flow in altering the thermodynamic mixing line (Section 3.1);

(*b*) temperature biases in atmospheric reanalysis or weather prediction datasets can shift the saturation threshold; and

(*c*) wind advection effects may displace a forming contrail outside the camera's field of view before it becomes optically visible, leading to apparent non-detections.

4. Conclusions

We performed a detailed study of a false-negative contrail case identified by all-sky ground-based camera imagery, flight-tracked trajectories, and weather reanalysis data. This case was analyzed using two levels of modeling fidelity: the SAC and LES with a contrail-adapted solver. LES results indicate that the bypass flow effects reduce the likelihood of contrail formation, suggesting that the SAC-based thermodynamic assumption may overestimate formation potential. The most plausible explanation for the false-negative case lies in altitude measurement inaccuracies and temperature biases in the weather data. Specifically, while barometric altitude yielded a low probability of contrail formation, the GPS-based altitude—typically less reliable at cruise level—predicted a higher likelihood (78–93%).

A variance-based Sobol sensitivity analysis of 764 flights confirmed that atmospheric temperature is the dominant first-order contributor to contrail formation predictions based on the SAC and on the initial conditions for LES. The second most influential factors are overall propulsive efficiency for the SAC approach and core radius for the LES-IC approach, both linked to the concentration of water vapor in the jet plume.

A contrail probability analysis for 248 flights with visual verification demonstrated consistent trends between the SAC and LES-IC frameworks, with both approaches exhibiting a tendency to overpredict contrail formation. This bias was attributed to the simplified treatment of the mixing process—namely, the neglect of bypass flow effects or assumption of fully mixed exhaust—as well as to temperature biases in reanalysis data and possibly wind advection, which can transport forming contrails out of the observational region.

Overall, these results emphasize that even small thermodynamic uncertainties—notably

in temperature and altitude—can significantly affect contrail formation predictions. The current parameter space, limited to a single narrowbody aircraft–engine configuration, underrepresents the diversity of operational conditions.

Future work would focus on (i) a more detailed characterization of parameter and measurement uncertainties, (ii) expanding the analysis to multiple aircraft and engine types, (iii) extending the dataset to additional days and regions to capture seasonal variability, and (iv) incorporating wind advection and bypass-flow effects.

Acknowledgments

The support of ONR to CTR under grant N000142312833 is gratefully acknowledged. The authors acknowledge the all-sky ground-based camera imagery captured by Reuniwatt and provided by both Reuniwatt and EUROCONTROL for research purposes. This work used computational resources from Expanse at San Diego Supercomputer Center through allocation EES230017 from the Advanced Cyberinfrastructure Coordination Ecosystem: Services & Support (ACCESS) program, which is supported by National Science Foundation grants #2138259, #2138286, #2138307, #2137603, and #2138296 (Boerner *et al.* 2023). We also thank Tony Zahtila for his insightful review.

REFERENCES

Boerner, T. J., Deems, S., Furlani, T. R., Knuth, S. L. & Towns, J. 2023 ACCESS: advancing innovation: NSF's advanced cyberinfrastructure coordination ecosystem: services & support. In Sinkovits, R. *et al.* (Eds.), *PEARC '23: Practice and Experience in Advanced Research Computing* (pp. 173–176). Assoc. Comput. Mach.

Brès, G. A., Bose, S. T., Emory, M., Ham, F. E., Schmidt, O. T., Rigas, G. & Colonius, T. 2018 Large-eddy simulations of co-annular turbulent jet using a Voronoi-based mesh generation framework. 2018-3302.

Ferreira, T., Alonso, J. & Gorlé, C. 2025 Large eddy simulation of the early jet-vortex interaction phase of contrails from hydrogen aircraft. AIAA AVIATION FORUM AND ASCEND 2025, Paper 2025-3032.

Ferreira, T., Alonso, J. J. & Gorlé, C. 2024*a* Developing a numerical framework for the high-fidelity simulation of contrails: Sensitivity analysis for conventional contrails. AIAA AVIATION FORUM AND ASCEND 2025, Paper 2024-3775.

Ferreira, T., Caprace, D.-G., Paoli, R., Shariff, K. & Lele, S. 2024*b* Can inducing the Crow instability reduce contrail radiative forcing? In *Proceedings of the Summer Program*, Center for Turbulence Research, Stanford University, pp. 13–22.

Gierens, K., Matthes, S. & Rohs, S. 2020 How well can persistent contrails be predicted? *Aerospace* **7**, 169.

Kärcher, B. 2018 Formation and radiative forcing of contrail cirrus. *Nat. Commun.* **9**, 1824.

Lee, D. S., Fahey, D. W. *et al.* 2021 The contribution of global aviation to anthropogenic climate forcing for 2000 to 2018. *Atmos. Environ.* **244**, 117834.

Lewellen, D. C. 2020 A large-eddy simulation study of contrail ice number formation. *J. Atmos. Sci.* **77**, 2585–2604.

Low, J., Teoh, R., Ponsonby, J., Gryspeerdt, E., Shapiro, M. & Stet-

tler, M. E. 2025 Ground-based contrail observations: comparisons with reanalysis weather data and contrail model simulations. *Atmos. Meas. Tech.* **18**, 37–56.

Lu, W., Zahtila, T., Chan, L., Nguyen, Q. D., Lei, C., Iaccarino, G. & Ooi, A. 2025 Modeling of uncertainties from spanwise asymmetries in upstream conditions and measurement plane location for flow past a circular cylinder confined within a duct. *Phys. Rev. Fluids* **10**, 064601.

Mannstein, H., Brömser, A. & Bugliaro, L. 2010 Ground-based observations for the validation of contrails and cirrus detection in satellite imagery. *Atmos. Meas. Tech.* **3**, 655–669.

Naiman, A., Lele, S. & Jacobson, M. 2011 Large eddy simulations of contrail development: sensitivity to initial and ambient conditions over first twenty minutes. *J. Geophys. Res. Atmos.* **116**, 2011JD015806.

Olive, X. 2019 traffic, a toolbox for processing and analysing air traffic data. *J. Open Source Softw.* **4**, 1518.

Paoli, R., Helie, J. & Poinsot, T. 2004 Contrail formation in aircraft wakes. *J. Fluid Mech.* **502**, 361–373.

Paoli, R., Nybelen, L., Picot, J. & Cariolle, D. 2013 Effects of jet/vortex interaction on contrail formation in supersaturated conditions. *Phys. Fluids* **25**.

Quibén Figueroa, R., Ferreira, T., Gorlé, C. & Soler Arnedo, M. 2025 Comparing high-fidelity LES of early contrail formation with ground-based images. Conference presentation, EGU General Assembly 2025, Vienna, Austria.

Schäfer, M., Strohmeier, M., Lenders, V., Martinovic, I. & Wilhelm, M. 2014 Bringing up OpenSky: a large-scale ADS-B sensor network for research. In *IPSN-14 Proceedings of the 13th International Symposium on Information Processing in Sensor Networks* (pp. 83–94). IEEE.

Schumann, U. 1996 On conditions for contrail formation from aircraft exhausts. *Meteorol. Z.* **5**, 4–23.

Schumann, U. 2012 *Atmospheric Physics: Background–Methods–Trends*. Springer.

Schumann, U., Hempel, R., Flentje, H., Garhammer, M., Graf, K., Kox, S., Lösslein, H. & Mayer, B. 2013 Contrail study with ground-based cameras. *Atmos. Meas. Tech.* **6**, 3597–3612.

Sobol, I. M. 2001 Global sensitivity indices for nonlinear mathematical models and their Monte Carlo estimates. *Math. Comput. Simul.* **55**, 271–280.

Teoh, R., Schumann, U., Gryspeerdt, E., Shapiro, M., Molloy, J., Koudis, G., Voigt, C. & Stettler, M. E. 2022 Aviation contrail climate effects in the North Atlantic from 2016 to 2021. *Atmos. Chem. Phys.* **22**, 10919–10935.